Resolving taphonomic and preparation biases in silicified faunas through paired acid residues and X-ray microscopy

Gabriel S. Jacobs [1, 2], **Sarah M. Jacquet** [2], **Tara Selly** [2, 3], **James D. Schiffbauer** [2, 3], **John Warren Huntley** [Corresp. 2]

[1] Department of Geology, Cornell College, Mount Vernon, IA, USA

[2] Department of Geological Sciences, University of Missouri, Columbia, MO, United States

[3] X-ray Microanalysis Laboratory, University of Missouri, Columbia, MO, United States

Corresponding Author: John Warren Huntley
Email address: huntleyj@missouri.edu

Paired petrography and acid maceration has shown that preferential silicification of shelly faunas can bias recovery based on taxon and body size. Here, silicified fossils from the Upper Ordovician Edinburg Formation, Strasburg Junction, Virginia, USA, were analyzed using X-ray tomographic microscopy (µCT) in conjunction with recovered residues from acid maceration of the same materials to further examine sources of potential bias. Results reveal that very small (< ~1 mm) fossils are poorly resolved in µCT when scanning at lower resolutions (~30µm), underestimating abundance of taxa including ostracods and bryozoans. Acid maceration, meanwhile, fails to recover poorly silicified fossils prone to disarticulation and/or fragmentation during digestion. Tests for patterns of breakage, however, indicate no significant size or taxonomic bias during extraction. Comparisons of individual fossils from 3-D fossil renders and maceration residues reveal patterns of fragmentation that are taxon-specific and allow the differentiation of biostratinomic and preparational breakage. Multivariate ordinations and cluster analyses of µCT and residue data in general produce concordant results but indicate that the variation in taxonomic composition of our samples is compromised by the resolvability of small size classes in µCT imaging, limiting the utility of this method for addressing paleoecological questions in these specific samples. We suggest that comparability of results will depend strongly on the sample size, taphonomic history, textural, and compositional characteristics of the samples in question, as well as µCT scan parameters. Additionally, applying these methods to different deposits will test the general applicability of the conclusions drawn on the relative strengths and weaknesses of the methods.

Resolving taphonomic and preparation biases in silicified faunas through paired acid residues and X-ray microscopy

Gabriel S. Jacobs[1,2], Sarah M. Jacquet[1], Tara Selly[1,3], James D. Schiffbauer[1,3], John Warren Huntley[1]

[1] Department of Geological Sciences, University of Missouri, Columbia, MO, USA

[2] Department of Geology, Cornell College, Mount Vernon, IA, USA

[3] X-ray Microanalysis Laboratory, University of Missouri, Columbia, MO, USA

Corresponding Author:

John Warren Huntley[1]

101 Geological Sciences Building, University of Missouri, Columbia, MO 65211, USA

Email address: huntleyj@missouri.edu

Abstract

Paired petrography and acid maceration has shown that preferential silicification of shelly faunas can bias recovery based on taxon and body size. Here, silicified fossils from the Upper Ordovician Edinburg Formation, Strasburg Junction, Virginia, USA, were analyzed using X-ray tomographic microscopy (μCT) in conjunction with recovered residues from acid maceration of the same materials to further examine sources of potential bias. Results reveal that very small (< ~1 mm) fossils are poorly resolved in μCT when scanning at lower resolutions (~30μm), underestimating abundance of taxa including ostracods and bryozoans. Acid maceration, meanwhile, fails to recover poorly silicified fossils prone to disarticulation and/or fragmentation during digestion. Tests for patterns of breakage, however, indicate no significant size or taxonomic bias during extraction. Comparisons of individual fossils from 3-D fossil renders and maceration residues reveal patterns of fragmentation that are taxon-specific and allow the differentiation of biostratinomic and preparational breakage. Multivariate ordinations and cluster analyses of μCT and residue data in general produce concordant results but indicate that the variation in taxonomic composition of our samples is compromised by the resolvability of small size classes in μCT imaging, limiting the utility of this method for addressing paleoecological questions in these specific samples. We suggest that comparability of results will depend strongly on the sample size, taphonomic history, textural, and compositional characteristics of the samples in question, as well as μCT scan parameters. Additionally, applying these methods to different deposits will test the general applicability of the conclusions drawn on the relative strengths and weaknesses of the methods.

Introduction

Silicification is a common preservational mode in the fossil record, especially in the early Paleozoic (Butts, 2007; Butts & Briggs, 2010), involving the fabric-specific replacement of calcareous biota (calcite and aragonite) with silica, typically as chalcedony (fine-grained fibrous quartz), opaline silica, or sometimes as sparry (macrocrystalline) quartz cement. While the fine-scale mechanisms of silicification in limestone remain unclear, the overall process is simple: pore fluids containing dissolved silica (whether volcanic, hydrothermal, or biogenic in origin) undergo transport and react with the host rock, causing contemporaneous dissolution of calcite and/or aragonite and the precipitation of silica through mechanisms involving pH change, increased temperature due to burial depth, and pressure dissolution (Kastner, Keene & Gieskes, 1977; Maliva & Siever, 1988).

Due to their enhanced resistance to other fabric-destructive diagenetic process (Schubert, Kidder & Erwin, 1997), silicified fossils are typically preserved in great fidelity and abundance. Moreover, the replacement process frequently replicates fine morphological details if not internal microstructure, and the insolubility of silica to dissolution by acid allows such material to be prepared chemically rather than mechanically (Baars, 2008; Butts, 2014). Acid maceration is a broadly employed technique used to extract silicified fossils from limestone, relying on the high solubility of calcite in acidic solution and the comparatively low resistance of micritic matrix to alteration or dissolution (St. Clair, 1935; Grant, 1989). However, such extraction methods can introduce potential biases that might skew perceptions of paleoecological studies investigating silicified specimens (Pruss, Payne & Westacott, 2015). Two primary sources of bias that can readily be identified include the differential likelihood

that a given specimen will (1) silicify during diagenesis, and (2) once silicified, survive preparation and be recovered.

If biases in differential preservation and recovery methods go unaccounted for, certain types of analyses can be more severely affected. Systematic descriptions of organisms may be only mildly affected by the underrepresentation of some ontogenetic stages relative to others, but studies specific to the paleoecology or biofacies of an assemblage can suffer in quality due to their reliance on an accurate assessment of which biota are present in the deposit. For example, the near absence of a guild of predators or the preferential breakage of certain types of shell ornamentation might drastically alter the interpretation of trophic relationships and biotic interactions. Similarly, the loss of fossils in a certain size range during preparation can affect interpretations of biostratinomic processes. Because these biases may skew paleoecological interpretations of fossil assemblages, quantifying or at least constraining them can improve confidence in the results of research relying on this common preparatory method.

Previous research has attempted to account for preservational and preparation bias in acid maceration of silicified fossils. Pruss et al. (2015) compared the relative abundances of fossil taxa in 11 hand samples of the Triassic Virgin Limestone Member of the Moenkopi Formation, from which the authors made a petrographic thin section and extracted fossil specimens via buffered acetic acid maceration. In general, echinoderms and gastropods were disproportionally over-represented in residues while bivalves were more likely to be identified in thin-section point counts (Pruss, Payne & Westacott, 2015).

Two questions not addressed by the aforementioned study are those of body size bias and breakage patterns. Since analysis of petrographic thin sections can identify fossils by their taxonomic group but offers minimal useful information with respect to their dimensions, detecting differences in body size distribution between thin section grains and fossils recovered in residues is not feasible. Similarly, it is impossible to tell by extraction methods whether fossils in residues suffered damage during digestion and washing or whether the breakage occurred prior to burial. Because thin sections and residues do not record the same fossils but rather disjoint subsets of the total fossils within the hand sample, no true pre and post comparison can be made. Indeed, since both methods applied in the Pruss et al. (2015) study are destructive, a single fossil cannot be recorded by both. This inherent limitation can be avoided, however, by pairing a non-destructive whole-rock analytical method with acid maceration. X-ray tomographic microscopy (μCT) is well-suited to such an approach, allowing compositional and textural differences within a sample to be imaged as a grayscale representation of density variation in three dimensions, revealing fossil material within. By then subjecting the sample to acid maceration, individual fossils can be resolved and measured before and after chemical preparation, and any breakage or loss documented and quantified.

Herein, we employ a paired approach combining μCT-generated three-dimensional volume data of bulk rock samples with investigation of subsequently acid-extracted insoluble residues from the same scanned samples to test the hypothesis that smaller fossils would be disproportionately less likely to survive preparation and be recovered from acid-digested residues and to further assess and quantify introduced

biases and their implications for paleoecological studies. For this study, we used prepared cores of carbonate bulk rock samples from the Edinburg Formation of Virginia, USA, which is well-known to host abundant and diverse silicified Ordovician marine fossils (Whittington & Evitt, 1953; Kraft, 1962). The pervasive silicification of the fossils within this unit makes it amenable to delivering sufficient contrast between the skeletal material and the host matrix using µCT.

Materials & Methods

Geological Setting

The Edinburg Formation is an Upper Ordovician unit of massively bedded black limestone with occasional shale interbeds, representing deep ramp to basinal deposition at the northwest of the Taconic foreland basin system after drowning of shallower ramp carbonate facies including the underlying Lincolnshire Limestone (Holland & Patzkowsky, 1996). K-bentonites derived from Taconic volcanism are sporadically present in the sediments of the foreland basin and have been sampled for radiometric ages, most notably the Millbrig bed, which lies up section of the Edinburg in the Martinsburg Formation and has a U-Pb date of 452.86 Ma (Mitchell et al., 2004; Sell, Ainsaar & Leslie, 2013).

All samples in this study were collected from the Liberty Hall facies of the Edinburg Formation exposed at Strasburg Junction rail cut, a well-studied site in the Shenandoah Valley of Virginia (Fig. 1, Table 1; Cooper & Cooper, 1946; Whittington & Evitt, 1953; Read, 1980; Jacobs & Carlucci, 2019). Hand sample observations revealed two starkly different lithologies (Table 1). Rocks from Horizon 1, approximately 0.5 m above the contact between the Lincolnshire Limestone and Edinburg Formation, were

coarse-grained, with a sparry or dismicritic texture likely indicative of recrystallization during early diagenesis. Sparse fossils and possible intraclasts visible on fresh surfaces were weakly aligned with the direction of original bedding, suggesting directional sorting during deposition. Horizons 3, 4, 5, and 6 cropped out over 30 m up section (Table 1) and were finely grained with only occasional sparry or hematitic grains. Fossils, where visible on fresh or weathered surfaces, were oriented randomly to original bedding and comprised arthropods, brachiopods, and occasional crinoid ossicles. Rocks from these horizons also displayed heavy rinds on weathered surfaces, frequently stained rusty orange to pale yellow with iron oxides/oxyhydroxides.

Fossil Extraction

From five horizons with fossils visible on weathered surfaces, 15 samples were prepared as cylindrical cores (Table 1), approximately 2 cm in diameter and ranging from 1 to 4 cm in height, normal to bedding. Each core was imaged via X-ray tomographic microscopy (μCT) using a Zeiss Xradia 510 Versa X-ray microscope with an isotropic voxel size of approximately 30 μm, producing three-dimensional renders of the core interiors. All μCT scans were processed using Dragonfly software Build 941–v.4.2.2 for Windows, Object Research Systems (ORS) Inc, Montreal, Canada, 2018 (http://www.theobjects.com/dragonfly). Post-image processing within the software was conducted to reduce imaging artifacts using the Ring Removal and Median filters. Regions of high brightness (corresponding to high-density ferrous material) and low brightness (corresponding to low-density siliceous material) relative to the local background were thresholded and manually segmented, excluding regions at the very top and bottom of cores due to persistent boundary artifacts. Due to radial and

longitudinal variation in background brightness across the cores, multiple brightness thresholds were used to segment siliceous material in some cores; in such cases, the total siliceous volume is the union of the volumes from segmentation by the various thresholds. Segmented volumes for ferrous and siliceous material were refined by removing small (<100 voxel total volume) islands and were then partitioned into distinct regions-of-interest (ROIs), using 6-connectivity (voxels considered to be connected if sharing faces rather than only edges or vertices) for both purposes. Individual fossils and other objects were identified among these ROIs by visual inspection in 3-D representations of voxels and against individual 2-D projections of µCT imagery. In cases where a fragmentary or incompletely resolved fossil fell into multiple non-connected ROIs, those ROIs were merged into one; in cases where a single ROI contained multiple contiguous objects, it was manually partitioned.

After each core had been imaged with µCT, they were macerated in 10% acetic acid to dissolve calcareous material until fully disaggregated and no longer visibly evolving gas bubbles. Acetic acid was chosen over alternatives such as hydrochloric acid or formic acid to allow for slow dissolution and avoidance of fossil damage. Insoluble residues were washed with water and sonicated in 30-second intervals, iterating until the supernatant ran clear. This washing process was then repeated using Calgon solution (0.052 M $Na_6(PO_3)_6$, 0.286 M $NaHCO_3$) as a deflocculant, sonicating as before, until all loose clay was removed. Cleaned residues were then washed over a 250-µm sieve, oven dried, and picked for identifiable fossils.

Statistical Analyses

Following scanning and segmentation, each object resolved in the µCT data was measured for minimum, maximum, and mean three-dimensional Feret diameter. Fossils that could be confidently identified to at least the phylum level were scored for additional taxon-specific features and anatomical measurements (Table 2).

Fossils recovered from residues were photographed using a GIGAmacro Magnify2 Robotic Imaging System with Canon EOS Rebel T8i DSLR and Nikon T1 1× and 3× objectives. For large specimens, additional photographs were taken under a reflected light microscope (Nikon SMZ1500 tethered to a Nikon D600 DSLR) to record features not visible in top-down view. Photographs were processed and analyzed with FIJI/ImageJ software, using the Trainable Weka Segmentation plugin to isolate fossils against the image background (Andreola et al., 2004a, b; Schindelin et al., 2012). Each fossil was measured for minimum and maximum two-dimensional Feret diameter as well as taxon-specific measurements corresponding to those taken from µCT data (Table 2).

For each core, both the segmented µCT render and acid residues were counted for the total abundance of fossil specimens. Trilobites were identified to the family level based on their general geometry, furrow pattern, and, in residues, their prosopon. Trilobite material not reliably assignable to a single family was treated as a separate category. Prosopon and other textural features were not easily resolvable in the µCT dataset, and so were not generally considered for taxonomic assignment in counts based on µCT results. Bryozoans were morphologically classified by growth form either as thin-branching, thick-branching, or fenestrate. Ostracods, gastropods, and bivalves

were not further classified due their generally small sample size and coarse silicification, precluding the reliable identification of taxonomically relevant features.

Using R statistical software, datasets were subjected to NMDS in three dimensions based on the Bray-Curtis dissimilarity index, using the *metaMDS* function provided in the *vegan* package (Dixon, 2003; R Core Team, 2021). Sites with no counted fossils were excluded from the analysis. Further paleoecological analysis of taxon abundances within and between samples was performed using PAST statistical software, calculating ecological dominance within samples (Simpson's *D*) and assessing compositional similarity between samples using the Bray-Curtis index (Hammer & Harper, 2001, 2022).

Results

A total of 582 distinct objects were resolved via µCT, 460 as a low-opacity siliceous phase and 122 as a high-opacity ferrous phase. Of these, 241 siliceous objects and 14 ferrous objects were identifiable to at least a coarse taxonomic level, with the remaining 219 and 108 respectively left unidentified (Fig. 2). Siliceous fossils were dominated by trilobites (n = 225), of which slightly less than half (n = 99) could be confidently assigned to a family classification; including Asaphidae (c.f. *Isotelus*), Cheiruridae (*Ceraurus*), Metagnostidae (*Trinodus*), Pterygometopidae (*Calyptaulax*), Raphiophoridae (*Ampyx*, *Lonchodomas*), and Remopleurididae (*Remopleurides*), all of which are previously known from this site (Whittington & Evitt, 1953; Evitt, 1961). Non-trilobite siliceous material consisted of thin-branching and fenestrate bryozoans and a single valve from an ostracod. Ferrous fossils were mostly gastropods, with two bivalves, one possible thin-branching bryozoan, and one infilling of a raphiophorid cranidium (Table 3). This

cranidium was counted towards siliceous and ferrous µCT object totals due to being preserved as silicified cuticle filled in by moldic pyrite but was counted as one individual in taxon totals (Fig. 2D).

Residues yielded 1,349 recognizable objects, 1,222 preserved as silica, 125 as ferrous minerals (pyrite, hematite, and/or limonite), and the remaining two as other indeterminate materials (neither were identifiable as a fossil) (Fig. 3). Nearly all siliceous fossils were attributed to at least a coarse taxonomic level, with only 48 unidentifiable. Conversely, 113 of the ferrous objects could not be identified. Siliceous objects in residue were made up largely of trilobites, fragments of thin-branching bryozoans, and ostracods. All trilobite genera represented in µCT were found also in residues, along with trilobites from the family Odontopleuridae (c.f. *Ceratocephala*). The remainder consisted of thick-branching and fenestrate bryozoans along with occasional brachiopod fragments. Ferrous fossils were exclusively represented by gastropods, except for a single bivalve (Table 3).

Tests of Preparation Bias

A contingency table was constructed containing µCT identified specimens counts, broken down by taxonomic grouping and by presence or absence in residues. The relationship between taxon and recovery was investigated using Pearson's χ^2 test (Table 4). The only taxonomic group which deviated significantly ($p = 0.04$) from overall likelihood of recovery was Unidentified Trilobita—material clearly from trilobites but lacking anatomical features in µCT sufficient to assign it to a family—which, despite being identified in µCT, are disproportionately unlikely to be recovered in residues.

Application of Pearson's χ^2 test to total counts of taxa identified in μCT and in residue found strong support ($p = 1.89 \times 10^{-35}$) for different proportional abundances in the two preparation types (Table 5). Raphiophorids ($p = 1.99 \times 10^{-5}$), remopleuridids ($p = 0.02$), unidentified trilobites ($p = 9.92 \times 10^{-17}$), bivalves ($p = 0.02$), and gastropods ($p = 2.08 \times 10^{-4}$) are significantly more abundant in μCT, while thin-branching bryozoans ($p = 3.26 \times 10^{-14}$), thick-branching bryozoans ($p = 1.15 \times 10^{-3}$), and ostracods ($p = 1.27 \times 10^{-13}$) are significantly more abundant in residues.

The presence of size bias in the likelihood of recovery was evaluated using the Mann-Whitney U-test with a null hypothesis of no difference in medians and a standard threshold of significance of $\alpha = 0.05$ (Mann & Whitney, 1947). In comparisons between fossils identified in both μCT and residue and those identified in μCT but *not* in residue, there was no statistically significant difference of maximum ($p = 0.54$), minimum ($p = 0.09$), or mean ($p = 0.24$) Feret diameters, nor of elongation factor ($p = 0.16$) defined as the ratio of maximum to minimum Feret diameters. However, when testing overall distributions of size between all fossils identified in μCT and all those found in residue, the U-test found a dramatic difference in maximum Feret diameter ($p = 1.75 \times 10^{-79}$) between the medians of the two groups (3.98 mm for CT, 1.41 mm for residue).

Exploratory Paleoecological Ordinations

NMDS performed separately on the μCT (Table 6) and residue (Table 7) datasets resulted in ordinations with stress scores of 0.06 and 0.08, respectively (Fig. 4). Taxon loadings in both ordinations consistently grouped bivalves and gastropods nearby each other. Ordinations of both μCT and residues tended to group medium-sized benthic trilobites (raphiophorids, pterygometopids, and cheirurids) together along

with unidentified trilobite material (most of which likely derived from one of those families), with pelagic trilobites (remopleuridids) plotting closer to gastropods and bivalves. Asaphids, likely represented here by the extremely large benthic trilobite *Isotelus*, consistently fall near the latter cluster but are represented only by fragments of cuticle. The ordination position of agnostids, whose life habit remains controversial (Fortey & Owens, 1999), is inconsistent between µCT and residues, falling near the benthic and pelagic trilobite clusters in those analyses, respectively. In both cases, they are closely accompanied by ostracods (which can occupy pelagic or benthic niches and whose life habit was not interpreted in this study). Due to the extreme disparity between identification in µCT and recovery in residues of ostracods, their location within the ordination for µCT data is likely not informative.

Thin-branching and fenestrate bryozoans plotted relatively close together, forming an isolated cluster. Thick-branching bryozoans were not closely associated with the other two morphotypes in the residue ordination and were not detected in µCT.

Samples from individual horizons tended to fall near each other in loose association. Two main clusters are apparent in both residue and µCT ordinations: one characterized by low NMDS1 scores and dominated by bryozoans, and one with higher NMDS1 scores and dominated by arthropods (trilobites and ostracods).

For each sample, dominance was computed for both µCT (Table 6) and residue (Table 7) taxon totals, with 95% confidence intervals based on 9999 bootstrap replicates (Fig. 5). The results of this analysis differed notably between the two; µCT dominance values fell in a tight band between 0.25 and 0.40 (excepting two outliers with $n<3$), while residue dominance values had a bimodal distribution with one group of values between

0.40 and 0.65 and another falling between 0.15 and 0.30. (Fig. 5) Rarefaction curves were calculated for both µCT (Table 6) and residue (Table 7) counts of each sample using PAST (Hammer & Harper, 2022; Fig. 6). Curves were visually inspected for the presence of an inflection point as a rough qualitative assessment of sampling completeness; a sample's curve "leveling off" (sudden decrease in slope) is considered informal evidence that taxa in the true population are well-represented in the sample (Sanders, 1968; Raup, 1975). This inflection point was observed in residue counts from most samples (prominently in 03-C1, 03-C3, 04-C1, and 06-C3), but not in µCT counts. This suggests that the smaller total counts of individuals in µCT data are leading to the non-recovery of rarer taxa. Such under-sampling is a liability of ecological analyses based on those samples.

Cluster Analysis

Multivariate cluster analyses were performed in PAST to provide alternate metrics of similarity in the paleoecological composition of the samples, using the Bray-Curtis index as before (Bray & Curtis, 1957; Hammer & Harper, 2022). Dendrograms with branch length scaled to similarity were constructed for µCT counts, residue counts, and a combined dataset treating µCT and residue counts for each sample as two separate sites (Figs. 7 and 8). Cluster analysis of µCT counts grouped samples from Horizon 04, and treated Horizon 05 similarly, but scattered samples from Horizons 03 and 06 across the tree. Using residue data, Horizon 05 formed a cluster as before but Horizon 04 split, with cores 04-C2 and 04-C3 remaining close but 04-C1 further removed; Horizons 03 and 06 were dispersed as in the µCT tree. In both trees, samples

from Horizon 01 were far removed from other samples, tending to form a cluster basal to the rest of the samples.

The combined tree retains the general close groupings of the two individual trees due to sharing the same dissimilarity metric (Fig. 8). Notably, even for Horizons 01, 04, and 05 whose samples tended to cluster in both the µCT and residue trees, those clusters are not closely related in the overall analysis; there are few clear patterns in this tree, but µCT samples tend to cluster more closely with other µCT samples, and residue samples with residue samples, than do µCT and residue counts of the same sample or even of samples from the same horizon.

Discussion

Size and Taxon Effects on Recovery

We hypothesized at the outset of this study that body size would be negatively associated with likelihood of recovery in residues; larger fossils may be more susceptible to breakage, and larger organisms with thicker skeletal elements may not fully silicify, producing a brittle outer husk. However, the results of our analysis do not support this possible effect. While fossils recovered in residue have a smaller median body size than those resolved in µCT, this appears to be due not to preferential breakage of larger fossils during washing but rather disproportionate non-resolution of smaller fossils in µCT datasets. Rather than µCT acting as a baseline to test the biases of acid maceration based on body size, the results of this study suggest the opposite.

Overrepresentation with respect to the abundance of pyritized taxa (gastropods and bivalves) in µCT may be the result of the high contrast between iron-bearing phases and the matrix, making such fossils easier to resolve in µCT than otherwise-

comparable siliceous fossils. Alternatively, because most of the pyritized fossil materials represent internal molds, they may be harder to identify outside of the 3D context provided in µCT, where they remain within their shell. If the latter is the case, this likely reflects lower fidelity of moldic pyrite preservation than that of the replacive silicification. Results of the NMDS ordinations consistently plotted molluscan taxa nearby one another, which may reflect either a shared infaunal environment or instead early burial conditions conducive to pyritization in those deposits. However, the low abundance of bivalves (2 in µCT, 1 recovered from residues, always alongside multiple gastropods) makes this apparent association tenuous. It is noteworthy that disseminated pyritization in the form of non-fossil granules was present in several samples (e.g., 05-C4) that contained no mollusks, suggesting that the presence or absence of mollusks in a sample may reflect their abundance in the paleoenvironment and is not solely controlled by whether early burial chemistry allowed pyritization to proceed. Ostracods, meanwhile, are disproportionately overrepresented in residue due to their small size making them difficult to resolve in µCT at the resolution used in this study. Branching bryozoans also suffer from this, but their numbers in residue are likely inflated by fragmentation of large individuals into many smaller ones.

Nonrecovery Bias and Potential Causes

Revealing that the number of unidentified trilobite fossils recognized in µCT is significantly less likely to be recovered in residue is to be expected. Fragmentation and incomplete preservation are common causes for trilobite material to lack identifying characteristics, and both are likely to promote further breakage and degradation during washing by compromising the structural integrity of the sclerite. This may also influence

likelihood of recovery by impeding identification of the fossil in residue; a fragment of cuticle lacking identifying characteristics is less likely to be recognized as corresponding to an object observed in μCT, and minor breakage is likely to disrupt recognizable aspects of its outline and other key features.

Diagenetic biases arise from a variety of sources and are heavily dependent on shell microstructure, organic matter, and availability of reactive and replacive ions to the shell. It is well-documented that certain taxa are more susceptible to silicification than others, and, even within taxa, textural differences can make certain skeletal elements more likely to be preserved than others (Daley & Boyd, 1996; Cherns et al., 2011; Butts, 2014). Organic matter content within a shell also influences the likelihood of silicification by providing nucleation sites for the deposition of silica, though the chemistry of this is complex (Wallace, DeYoreo & Dove, 2009; Butts, 2014). Similarly, replacement via pyrite tends to initiate at sites of organic matrix in the shell but is also dependent upon reducing microenvironments and/or microbial zonation within the sediment (Fisher, 1986; Canfield & Raiswell, 1991; Schiffbauer et al., 2014).

Further biases can arise from the sample extraction and preparation process itself. During washing, larger fossils may be tumbled against other grains or container walls, leading to abrasion or breakage, while smaller fossils may be crushed beneath larger objects as grains settle. Elongated grains may be more prone to breakage than spheroidal grains of the same volume due to a lower minimum cross-sectional area, which can lead to taxon or sclerite bias against fossils with rod-like geometry, such as branching bryozoans and the spines of some trilobites. Breakage during preparation can cause taxa to be undercounted due to indiscriminate destruction of individuals or

damage sufficient to remove recognizable features. Paradoxically, it can also inflate taxon counts by turning one fossil into many still-recognizable fragments. These overlapping effects can produce a wide variety of biases in size and shape, and the cumulative effect on measurements of abundance cannot reasonably be predicted *a priori*.

The composition of the host rock can further impose preparation-related biases. For instance, well-cemented rocks frequently require longer maceration periods than poorly consolidated ones, while argillaceous rocks may need more thorough washing to drive off insoluble clays, often including sonication. The longer sediment is washed and manipulated, the more breakage tends to occur, making matrix texture an important factor of preparation bias. While the acid maceration processes can be accelerated by using alternative acids, such as hydrochloric, the violent effervescence caused by the intensity of the reaction can also have a deleterious effect on the extraction of delicate forms.

Artifacts and Limitations of µCT

While a powerful tool for visualization, µCT does present some unavoidable sources of potential error: artifacts arising from specimen capture and processing, particularly the "hardening" of the X-ray beam through preferential absorption of lower-energy photons by the sample. Beam hardening is a ubiquitous issue in µCT, but not all hardening artifacts are of equal impact. Since the beam is slightly hardened by passing through the outer surface of the sample, the interior is always slightly darkened relative to the outermost layer; these "cupping artifacts" are produced predictably based on sample

446 geometry and can be corrected relatively easily (Schladitz, 2011; Jung et al., 2011;
447 Abel, Laurini & Richter, 2012).

448 Heterogeneous samples may experience additional artifacts. Regions of higher-
449 density material (e.g., iron minerals in sediments, bones in biological samples) can
450 drastically harden beams passing through them, causing dark blotches to appear
451 around bright features within a sample and especially in the spaces between multiple
452 bright features. These artifacts are far more difficult to correct due to their irregular
453 shape and remain the subject of ongoing research in economic geology and other
454 materials science fields (Remeysen & Swennen, 2006; Park, Chung & Seo, 2015; Bam
455 et al., 2019). Given the abundant pyrite in the material examined in this study, this
456 stands as a caveat to the results reported here; similar methods applied to rocks with
457 lower density variation may yield clearer µCT data and therefore more complete
458 identification of fossils within the samples. Filtering during pre-processing, or correction
459 applications in post-processing software packages, can reliably improve these artifacts,
460 but often at the cost of introducing noise along the axis of sample rotation (Kyriakou,
461 Prell & Kalender, 2009; Yousuf & Asaduzzaman, 2009).

462 **Relevance for Paleoecological Interpretation**

463 Broad categories of biofacies are generally consistent between residue- and
464 µCT-derived taxon abundances as interpreted using NMDS. While total counts for µCT
465 are much lower than those of residues, relative abundances in the former largely
466 recapitulate the latter with some notable exceptions; ostracods are almost absent from
467 µCT data, due to resolution constraints imposed from the diameter of the cores, even
468 when highly abundant in residues, and bryozoan counts tend to be much higher in

residues than in μCT due to breakage transforming one large fragment into many small fragments. For this reason, the application of μCT data alone to describe paleoecological structure should be undertaken with caution. Ordinations used in paleoecology are sufficiently complex that such biases in recovery can, by introducing error and uncertainty upstream, irreparably taint conclusions drawn downstream.

Overall, the use of μCT counts on their own to characterize silicified remains in these limestone biofacies is of uncertain value. Sample volume constraints make bulk samples unfeasible, and the cost of instrument time can be a roadblock to replication and large-scale sampling. However, μCT may be best suited when chemical preparation is dangerous or impractical due to matrix or fossil mineralogy, or when studying sponges, bryozoans, corals, or other modular organisms for which fragmentation during washing can obscure or inflate the number of individuals present. Samples best suited to the approach outlined in this study will be densely fossiliferous (mitigating the limitation of sample volume), bear taxa with morphological features conducive to identification in μCT (related to shape rather than texture) and contain grains more susceptible to dissolution than the matrix or cement joining them together. Such rocks should also have a contrast in density, whereby the material of interest has a higher X-ray attenuation, for better visualization, whilst keeping in mind the potential effects of beam hardening artifacts. Conodonts and other phosphatic fossils, for example, are occasionally known from silicified sediments, and characterizing taxonomic assemblages using μCT techniques may constitute an alternative to digestion from the toxic and hazardous hydrofluoric acid normally used to extract fossils from siliceous cements (Green, 2001).

Conclusions

The main goal of this study was to quantify the effects of taxonomic affinity and body size on the likelihood of fossil recovery as revealed by different extraction methods. Breakage remains an unavoidable concern with acid maceration, one which µCT can provide insight to, though not without its own caveatsWhile µCT imaging of silicified fossils in limestone matrix can resolve morphological features of interest, the issues faced in this specific study may limit this technique's ability to answer broader paleoecological questions. Analyzing original rock contents as a means of detecting breakage during preparation may be valuable as a control on fragmentary abundance counts, but limitations of sample size and the potential for taxonomic bias to affect ordinations present serious pitfalls to analysis or characterization of biofacies. It can, however, be useful in establishing broad categories if not finer gradations between related assemblages. Since the drawbacks resulting from beam hardening and other µCT artifacts are heavily dependent on the properties of the sample, these methods may prove more effective when applied to rocks containing different fossil taxa or with different lithologic compositions from the materials studied here.

Variation in fossil recovery can stem not only from easily observable sedimentological features such as grain size and composition but also from redox chemistry and solute profiles of pore fluids during burial and early diagenesis, which can be challenging to infer from samples without more in-depth geochemical analyses. Original shell composition, both in terms of organic content and aragonitic versus calcitic (high- or low-magnesium) mineralogy is likely relevant due to its influence on the spontaneity and kinetics of silicification chemistry. Information on the breadth of

variation is limited but suggests a wide range of possible taxonomic outcomes based on sample lithology.

Acknowledgements

We gratefully acknowledge L.G. Huntley for assistance with fieldwork and William Foster, Agata Jurkowska, and an anonymous reviewer for their helpful commentary and suggested improvements.

Funding Statement

GSJ was supported by the Department of Geological Sciences, University of Missouri. JWH and GSJ were supported by NSF EAR CAREER 1650745. JDS, TS, and the X-ray Microanalysis Lab were supported by NSF Instrumentation and Facilities (EAR/IF) 1636643. SMJ and TS were supported by NSF Sedimentary Geology and Paleobiology Award (EAR-SGP) 1917031.

References

Abel R, Laurini C, Richter M. 2012. A palaeobiologist's guide to "virtual" micro-CT preparation. *Palaeontologia Electronica*. DOI: 10.26879/284.

Andreola F, Castellini E, Manfredini T, Romagnoli M. 2004a. The role of sodium hexametaphosphate in the dissolution process of kaolinite and kaolin. *Journal of the European Ceramic Society* 24:2113–2124. DOI: 10.1016/S0955-2219(03)00366-2.

Andreola F, Castellini E, Manfredini T, Romagnoli M. 2004b. The role of sodium hexametaphosphate in the dissolution process of kaolinite and kaolin. *Journal of the European Ceramic Society* 24:2113–2124. DOI: 10.1016/S0955-2219(03)00366-2.

Baars C. 2008. Acid digestion of silicified shells. *Geological Curator* 9:29–33. DOI: 10.55468/GC204.

Bam LC, Miller JA, Becker M, Basson IJ. 2019. X-ray computed tomography: Practical evaluation of beam hardening in iron ore samples. *Minerals Engineering* 131:206–215. DOI: 10.1016/j.mineng.2018.11.010.

Butts SH. 2007. Silicified Carboniferous (Chesterian) Brachiopoda of the Arco Hills Formation, Idaho. *Journal of Paleontology* 81:48–63.

Butts SH. 2014. Silicification. *The Paleontological Society Papers* 20:15–34. DOI: 10.1017/s1089332600002783.

554 Butts SH, Briggs DEG. 2010. Silicification Through Time. In: 411–434. DOI:
555 10.1007/978-90-481-8643-3_11.
556 Canfield DE, Raiswell R. 1991. Pyrite Formation and Fossil Preservation. In: 337–387.
557 DOI: 10.1007/978-1-4899-5034-5_7.
558 Cherns L, Wheeley J, Wright VP, Allison PA, Bottjer DJ. 2011. Taphonomic bias in
559 shelly faunas through time: Early aragonite dissolution and its implications for the
560 fossil record. In: *Taphonomy, Second Edition: Process and Bias Through Time;*
561 *Topics in Geobiology 32*.
562 Cooper BN, Cooper GA. 1946. Lower middle Ordovician stratigraphy of the
563 Shenandoah valley, Virginia. *Bulletin of the Geological Society of America* 57:35–
564 114.
565 Daley RL, Boyd DW. 1996. The Role of Skeletal Microstructure During Selective
566 Silicification of Brachiopods. *Journal of Sedimentary Research* 66:155–162. DOI:
567 10.1306/D42682E3-2B26-11D7-8648000102C1865D.
568 Dixon P. 2003. VEGAN, a package of R functions for community ecology. *Journal of*
569 *Vegetation Science* 14:927–930. DOI: 10.1111/j.1654-1103.2003.tb02228.x.
570 St. Clair, DW. 1935. The Use of Acetic Acid to Obtain Insoluble Residues. *SEPM*
571 *Journal of Sedimentary Research* Vol. 5. DOI: 10.1306/D4268F3B-2B26-11D7-
572 8648000102C1865D.
573 Elkhoury JE, Shankar R, Ramakrishnan TS. 2019. Resolution and Limitations of X-Ray
574 Micro-CT with Applications to Sandstones and Limestones. *Transport in Porous*
575 *Media* 129:413–425. DOI: 10.1007/s11242-019-01275-1.
576 Evitt WR. 1961. *Early Ontogeny in the Trilobite Family Asaphidae*.
577 Fisher IStJ. 1986. Pyrite replacement of mollusc shells from the Lower Oxford Clay
578 (Jurassic) of England. *Sedimentology* 33:575–585. DOI: 10.1111/j.1365-
579 3091.1986.tb00762.x.
580 Fortey RA, Owens RM. 1999. Feeding habits in trilobites. *Palaeontology* 42:429–465.
581 DOI: 10.1111/1475-4983.00080.
582 Grant RE. 1989. Extraction of fossils from carbonates by acid. *The Paleontological*
583 *Society Special Publications* 4:237–243. DOI: 10.1017/S2475262200005190.
584 Green OR. 2001. Extraction Techniques for Phosphatic Fossils. In: *A Manual of*
585 *Practical Laboratory and Field Techniques in Palaeobiology*. Dordrecht: Springer
586 Netherlands, 318–330. DOI: 10.1007/978-94-017-0581-3_27.
587 Hammer Ø, Harper DAT. 2001. PAST: Paleontological Statistics Software Package for
588 Education and Data Analysis. *Palaeontologica Electronica* 4:1–9.
589 Hammer Ø, Harper DAT. 2022. PAST.
590 Holland SM, Patzkowsky ME. 1996. Sequence stratigraphy and long-term
591 paleoceanographic change in the Middle and Upper Ordovician of the eastern
592 United States. In: *Paleozoic sequence stratigraphy; views from the North American*
593 *Craton*. Geological Society of America,. DOI: 10.1130/0-8137-2306-X.117.

Jacobs GS, Carlucci JR. 2019. Ontogeny and shape change of the phacopid trilobite Calyptaulax. *Journal of Paleontology* 93:1105–1125. DOI: 10.1017/jpa.2019.38.

Jung Y-J, Yun T-S, Kim K-Y, Choo J-H. 2011. Image Calibration Techniques for Removing Cupping and Ring Artifacts in X-ray Micro-CT Images. *Journal of the Korean Geotechnical Society* 27:93–101. DOI: 10.7843/kgs.2011.27.11.093.

Kastner M, Keene JB, Gieskes JM. 1977. Diagenesis of siliceous oozes—I. Chemical controls on the rate of opal-A to opal-CT transformation—an experimental study. *Geochimica et Cosmochimica Acta* 41:1041–1059. DOI: 10.1016/0016-7037(77)90099-0.

Kraft JC. 1962. Morphologic and systematic relationships of some Middle Ordovician Ostracoda. In: *GSA Memoirs*. New York: Geological Society of America, 1–119. DOI: 10.1130/MEM86-p1.

Kyriakou Y, Prell D, Kalender WA. 2009. Ring artifact correction for high-resolution micro CT. *Physics in Medicine and Biology* 54:N385–N391. DOI: 10.1088/0031-9155/54/17/N02.

Maliva RG, Siever R. 1988. Mechanism and Controls of Silicification of Fossils in Limestones. *The Journal of Geology* 96:387–398. DOI: 10.1086/629235.

Mann HB, Whitney DR. 1947. On a Test of Whether one of Two Random Variables is Stochastically Larger than the Other. *The Annals of Mathematical Statistics* 18:50–60. DOI: 10.1214/aoms/1177730491.

Mitchell CE, Adhya S, Bergström SM, Joy MP, Delano JW. 2004. Discovery of the Ordovician Millbrig K-bentonite Bed in the Trenton Group of New York State: implications for regional correlation and sequence stratigraphy in eastern North America. *Palaeogeography, Palaeoclimatology, Palaeoecology* 210:331–346. DOI: 10.1016/j.palaeo.2004.02.037.

Park HS, Chung YE, Seo JK. 2015. Computed tomographic beam-hardening artefacts: mathematical characterization and analysis. *Philosophical Transactions of the Royal Society A: Mathematical, Physical and Engineering Sciences* 373:20140388. DOI: 10.1098/rsta.2014.0388.

Pruss SB, Payne JL, Westacott S. 2015. Taphonomic bias of selective silicification revealed by paired petrographic and insoluble residue analysis. *Palaios* 30:620–626. DOI: 10.2110/palo.2014.105.

R Core Team. 2021. R: A language and environment for statistical computing.

Read JF. 1980. Carbonate ramp-to-basin transitions and foreland basin evolution, Middle Ordovician, Virginia Appalachians. *The American Association of Petroleum Geologists Bulletin* 64:1575–1612.

Remeysen K, Swennen R. 2006. Beam hardening artifact reduction in microfocus computed tomography for improved quantitative coal characterization. *International Journal of Coal Geology* 67:101–111. DOI: 10.1016/j.coal.2005.10.001.

Schiffbauer JD, Xiao S, Cai Y, Wallace AF, Hua H, Hunter J, Xu H, Peng Y, Kaufman AJ. 2014. A unifying model for Neoproterozoic–Palaeozoic exceptional fossil preservation through pyritization and carbonaceous compression. *Nature Communications* 5:5754. DOI: 10.1038/ncomms6754.

Schindelin J, Arganda-Carreras I, Frise E, Kaynig V, Longair M, Pietzsch T, Preibisch S, Rueden C, Saalfeld S, Schmid B, Tinevez J-Y, White DJ, Hartenstein V, Eliceiri K, Tomancak P, Cardona A. 2012. Fiji: an open-source platform for biological-image analysis. *Nature Methods* 9:676–682. DOI: 10.1038/nmeth.2019.

Schladitz K. 2011. Quantitative micro-CT. *Journal of Microscopy* 243:111–117. DOI: 10.1111/j.1365-2818.2011.03513.x.

Schubert JK, Kidder DL, Erwin DH. 1997. Silica-replaced fossils through the Phanerozoic. *Geology* 25:1031–1034.

Sell B, Ainsaar L, Leslie S. 2013. Precise timing of the Late Ordovician (Sandbian) super-eruptions and associated environmental, biological, and climatological events. *Journal of the Geological Society* 170:711–714. DOI: 10.1144/jgs2012-148.

Wallace AF, DeYoreo JJ, Dove PM. 2009. Kinetics of Silica Nucleation on Carboxyl- and Amine-Terminated Surfaces: Insights for Biomineralization. *Journal of the American Chemical Society* 131:5244–5250. DOI: 10.1021/ja809486b.

Whittington HB, Evitt WRI. 1953. Silicified Middle Ordovician Trilobites. *Geological Society of America Memoirs* 59:1–137. DOI: 10.1130/MEM59.

Yousuf MA, Asaduzzaman M. 2009. An Efficient Ring Artifact Reduction Method Based on Projection Data for Micro-CT Images. *Journal of Scientific Research* 2:37–45. DOI: 10.3329/jsr.v2i1.2645.

673 Figure 1. Location map and generalized stratigraphy of samples analyzed in this study.
674 Adapted from Jacobs and Carlucci (2019).
675
676 Figure 2. µCT renderings of fossils identified in cores of the Edinburg Formation. Blue
677 indicates silica and red and pink indicate Fe-rich mineralization. A) Fenestrate bryozoan
678 (01-C4-001). B) Nuculanid bivalve (03-C3-064) with three small gastropods (03-C3-060,
679 03-C3-062, 03-C3-065) in pink. C) Closer view of gastropod (03-C3-060). D)
680 Raphiophorid cranidium preserved in silica (05-C4-005) with pyrite infilling (05-C4-047).
681 E) Pterygometopid cephalon (04-C2-028). Note the compound eyes. F) Agnostid
682 fragment (06-C4-027). G) Pterygometopid pygidium (05-C1-019). All scale bars
683 approximate 1 mm.
684
685 Figure 3. Photomicrographs and SEM images of fossils recovered in macerate residues.
686 A) Silicified fenestrate bryozoan (01-C1). B) Silicified erect branching bryozoan (03-C3).
687 C) Pyritized gastropod (03-C3). D) Silicified raphiophorid cranidium (03-C1). E) Silicified
688 *Calyptaulax* cranidium (06-C4). F) Silicified agnostid fragment (06-C4). G) Silicified
689 *Calyptaulax* pygidium (03-C1). H) SEM-image of silicified ostracod valve (04-C1). I)
690 SEM image of silicified trilobite pygidium (04-C1).
691
692 Figure 4. Results of NMDS of taxon abundance data for A) µCT data (stress = 0.06) and
693 B) acid maceration residue data (stress = 0.08). Samples are plotted as grey squares.
694 Taxon scores are indicated by blue circles. Convex hulls contain samples from each
695 sampling horizon (Table 1). Red: EB18-01. Orange: EB18-03. Yellow: EB18-04. Green:
696 EB18-05. Blue: EB18-06.
697
698 Figure 5. Simpson's Dominance (D) and bootstrapped 95% confidence intervals
699 calculated for each sample by data type. µCT data are in blue and acid maceration
700 residue data are in orange.
701
702 Figure 6. Rarefaction analysis of taxonomic richness for A) µCT samples (Table 6) and
703 B) acid maceration residue samples (Table 7).
704
705 Figure 7. Bray-Curtis similarity dendrograms of taxon abundance values in A) µCT
706 samples (Table 6) and B) acid maceration residue samples (Table 7) calculated
707 separately.

Figure 1

Figure 1

Figure 1. Location map and generalized stratigraphy of samples analyzed in this study. Adapted from Jacobs and Carlucci (2019).

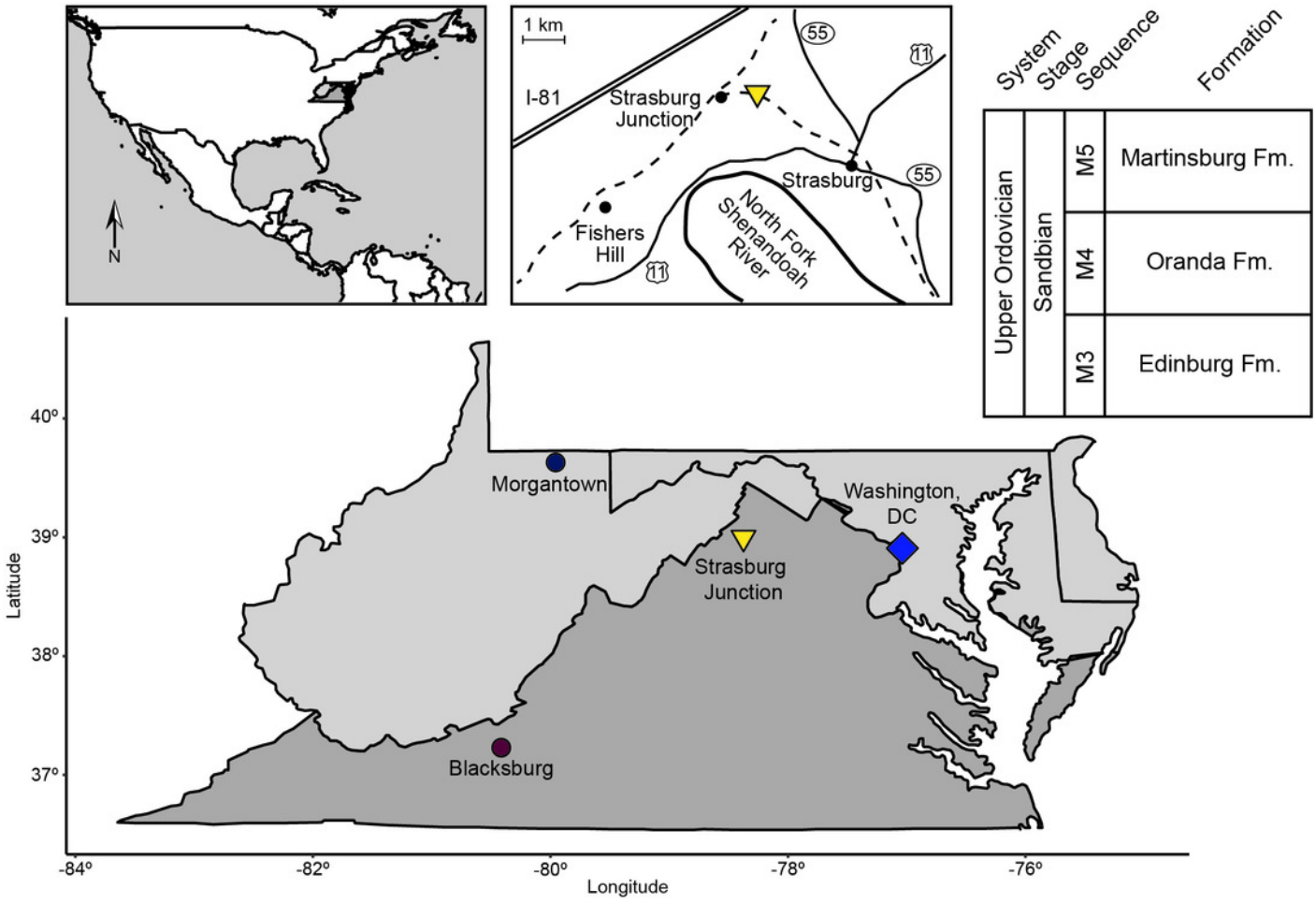

Figure 2

Figure 2

Figure 2. CT renderings of fossils identified in cores of the Edinburg Formation. Blue indicates silica and red and pink indicate Fe-rich mineralization. A) Fenestrate bryozoan (01-C4-001). B) Nuculanid bivalve (03-C3-064) with three small gastropods (03-C3-060, 03-C3-062, 03-C3-065) in pink. C) Closer view of gastropod (03-C3-060). D) Raphiophorid cranidium preserved in silica (05-C4-005) with pyrite infilling (05-C4-047). E) Pterygometopid cephalon (04-C2-028). Note the compound eyes. F) Agnostid fragment (06-C4-027). G) Pterygometopid pygidium (05-C1-019). All scale bars approximate 1 mm.

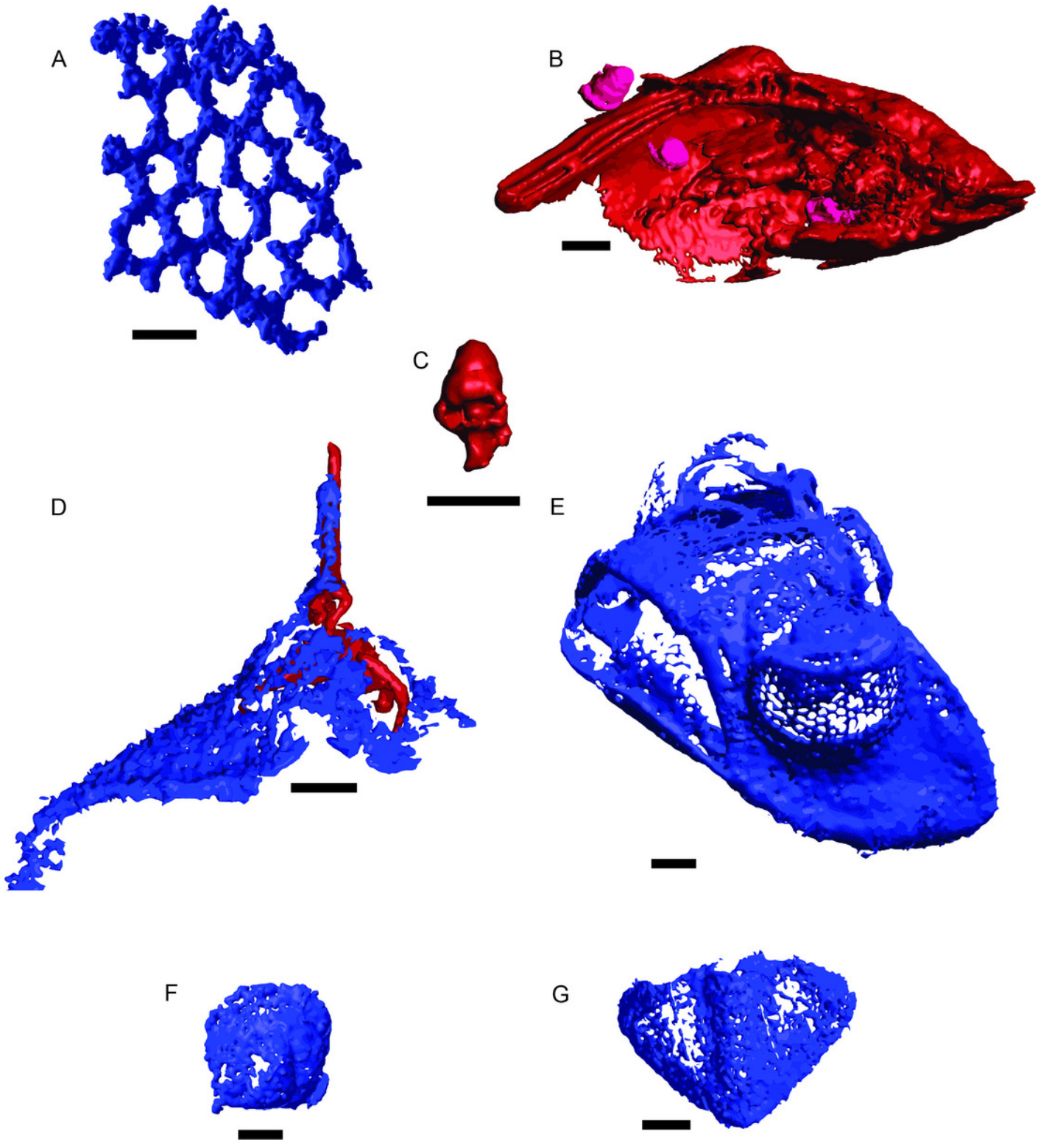
A
B
C
D
E
F
G

Figure 3

Figure 3

Figure 3. Photomicrographs and SEM images of fossils recovered in macerate residues. A) Silicified fenestrate bryozoan (01-C1). B) Silicified erect branching bryozoan (03-C3). C) Pyritized gastropod (03-C3). D) Silicified raphiophorid cranidium (03-C1). E) Silicified *Calyptaulax* cranidium (06-C4). F) Silicified agnostid fragment (06-C4). G) Silicified *Calyptaulax* pygidium (03-C1). H) SEM-image of silicified ostracod valve (04-C1). I) SEM-image of silicified trilobite pygidium (04-C1).

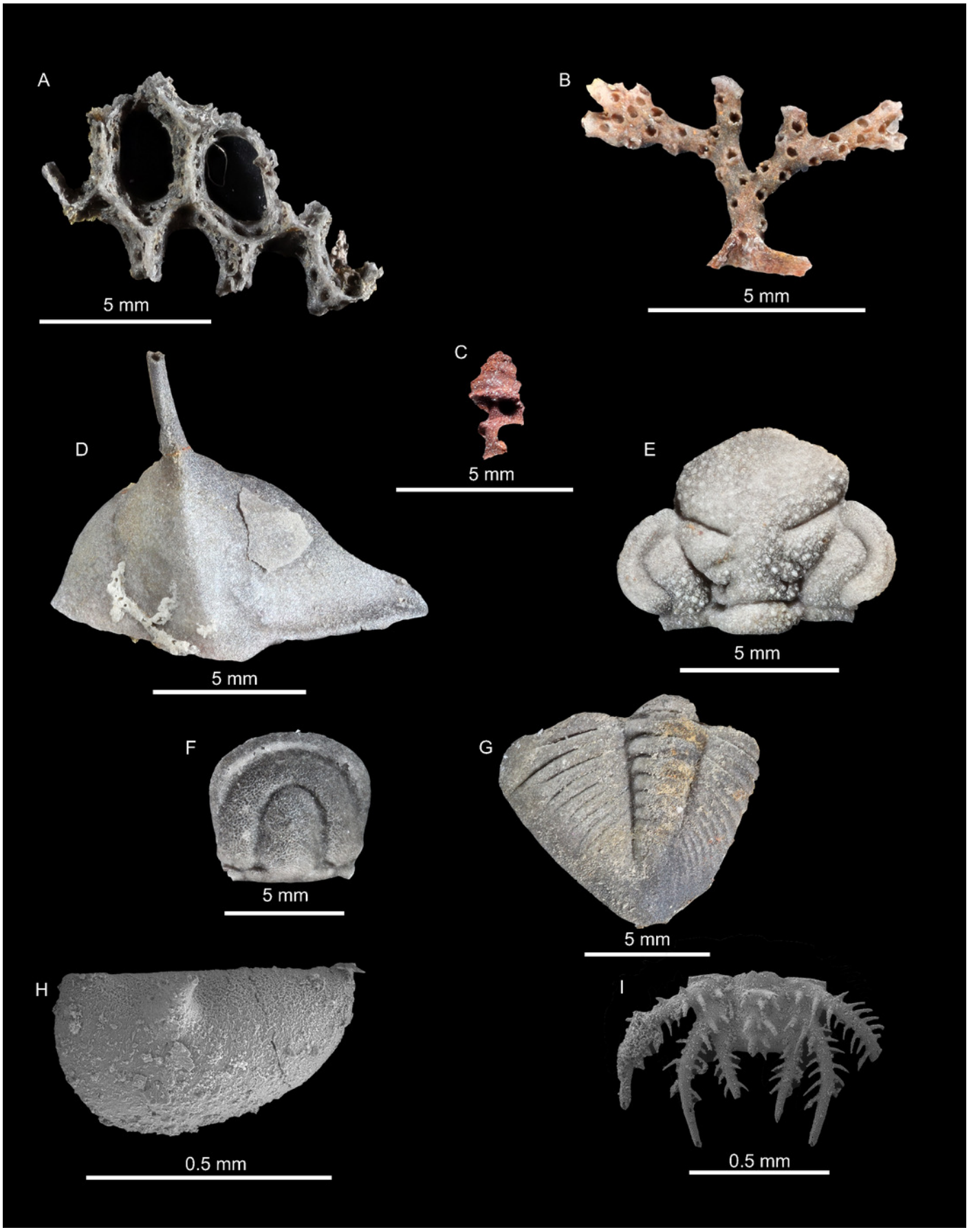
A
5 mm
B
5 mm
C
5 mm
D
5 mm
E
5 mm
F
5 mm
G
5 mm
H
0.5 mm
I
0.5 mm

Figure 4

Fig 4

Figure 4. Results of NMDS of taxon abundance data for A) µCT data (stress = 0.06) and B) acid maceration residue data (stress = 0.08). Samples are plotted as grey squares. Taxon scores are indicated by blue circles. Convex hulls contain samples from each sampling horizon (Table 1). Red: EB18-01. Orange: EB18-03. Yellow: EB18-04. Green: EB18-05. Blue: EB18-06.

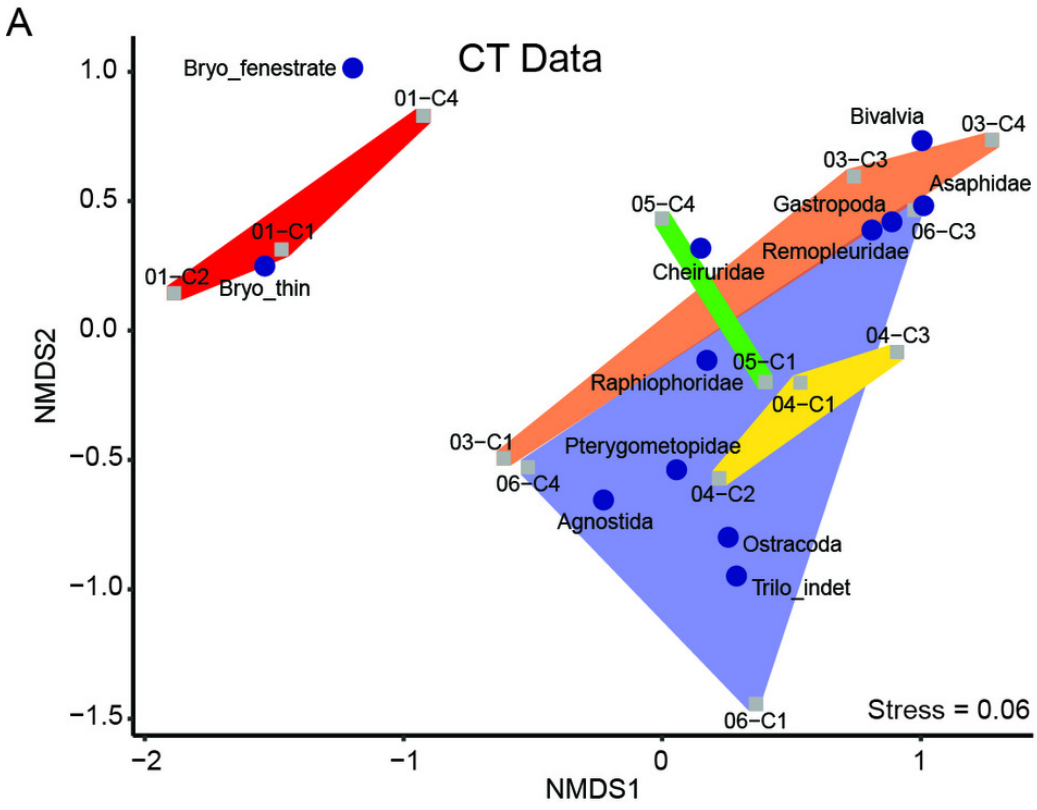
A
CT Data
Bryo_fenestrate
01−C4
01−C1
01−C2
Bryo_thin
Bivalvia
03−C4
03−C3
Asaphidae
05−C4
Gastropoda
06−C3
Remopleuridae
Cheiruridae
04−C3
05−C1
Raphiophoridae
04−C1
03−C1
Pterygometopidae
06−C4
04−C2
Agnostida
Ostracoda
Trilo_indet
06−C1
Stress = 0.06
NMDS1
NMDS2
1.0
0.5
0.0
−0.5
−1.0
−1.5
−2
−1
0
1

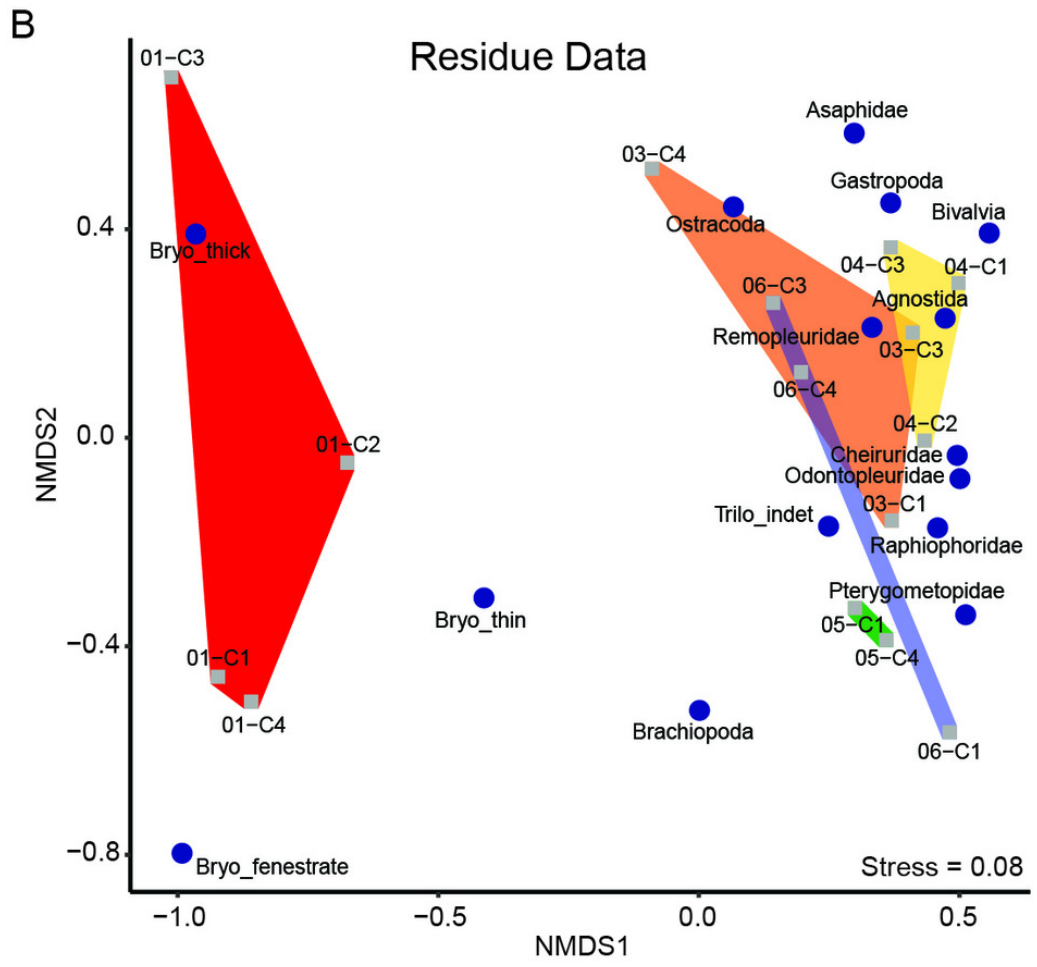
B
Residue Data
01−C3
Bryo_thick
01−C2
01−C1
01−C4
Bryo_fenestrate
Bryo_thin
Asaphidae
03−C4
Gastropoda
Ostracoda
Bivalvia
04−C3
04−C1
06−C3
Agnostida
Remopleuridae
03−C3
06−C4
04−C2
Cheiruridae
Odontopleuridae
03−C1
Trilo_indet
Raphiophoridae
Pterygometopidae
05−C1
05−C4
Brachiopoda
06−C1
Stress = 0.08
NMDS1
NMDS2
0.4
0.0
−0.4
−0.8
−1.0
−0.5
0.0
0.5

Figure 5

Fig 5

Figure 5. Simpson's Dominance (D) and bootstrapped 95% confidence intervals calculated for each sample by data type. data are in blue and acid maceration residue data are in orange.

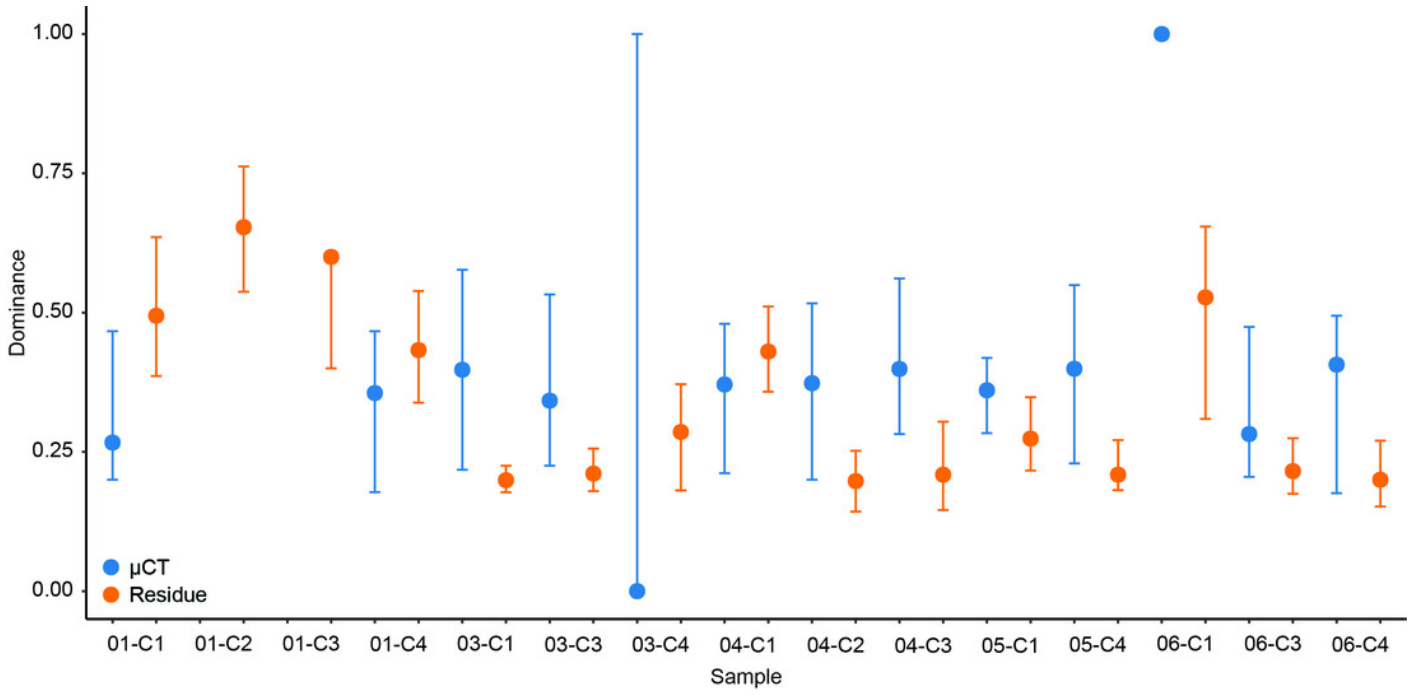

Figure 6

Fig 6

Figure 6. Rarefaction analysis of taxonomic richness for A) µCT samples (Table 6) and B) acid maceration residue samples (Table 7).

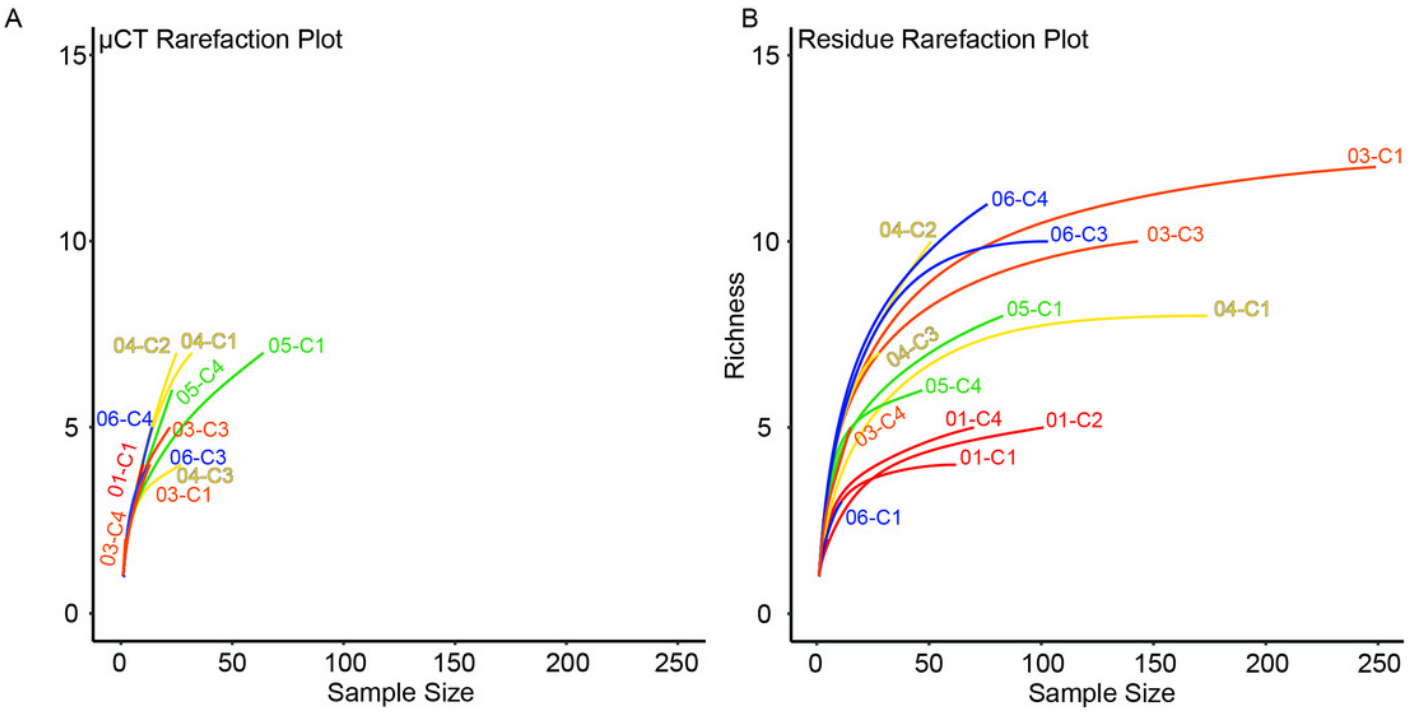

Figure 7

Fig 7

Figure 7. Bray-Curtis similarity dendrograms of taxon abundance values in A) µCT samples (Table 6) and B) acid maceration residue samples (Table 7) calculated separately.

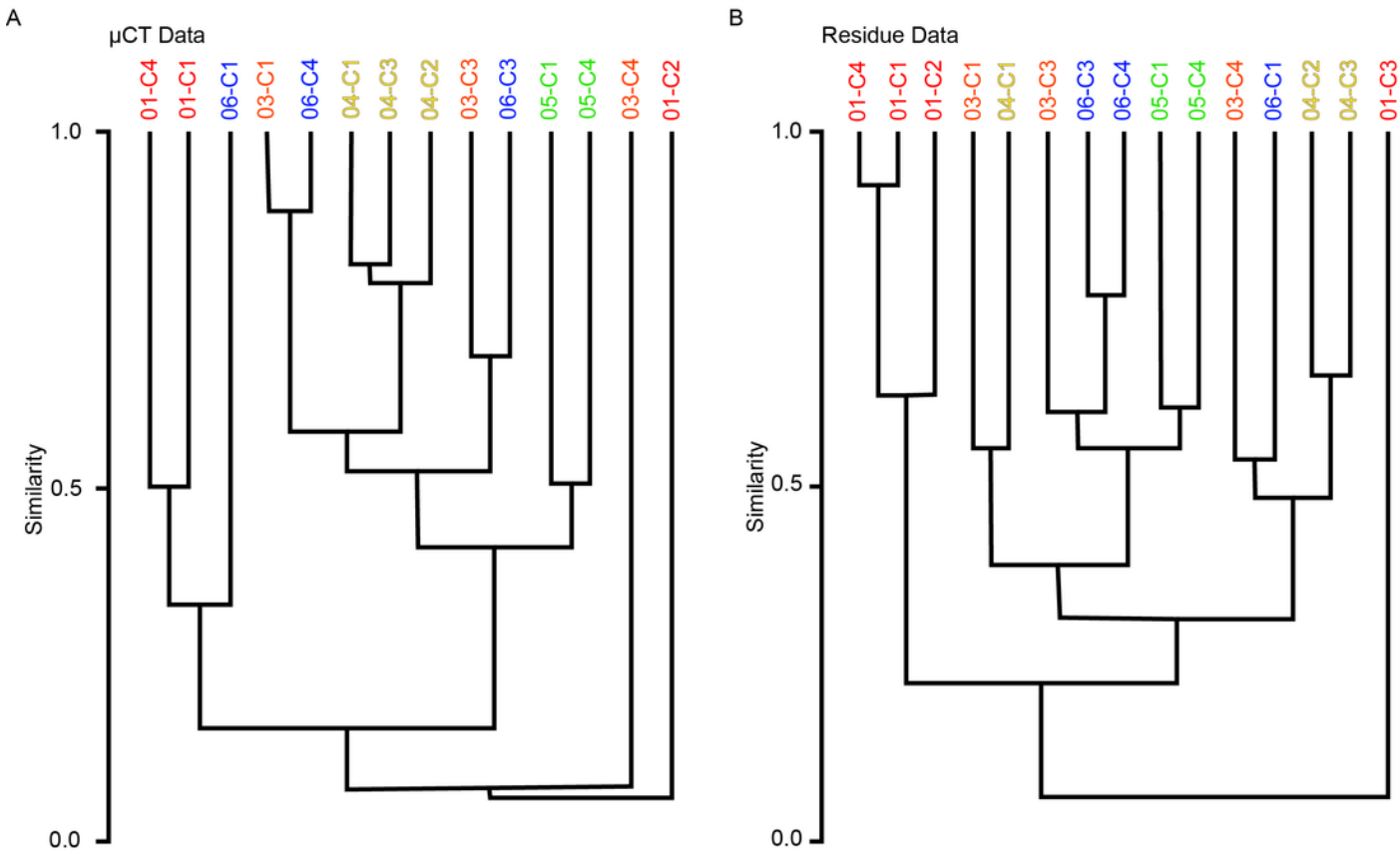

Figure 8

Fig 8

Figure 8. Bray-Curtis similarity dendrograms of pooled taxon abundance values in µCT samples (Table 6) and acid maceration residue samples (Table 7).

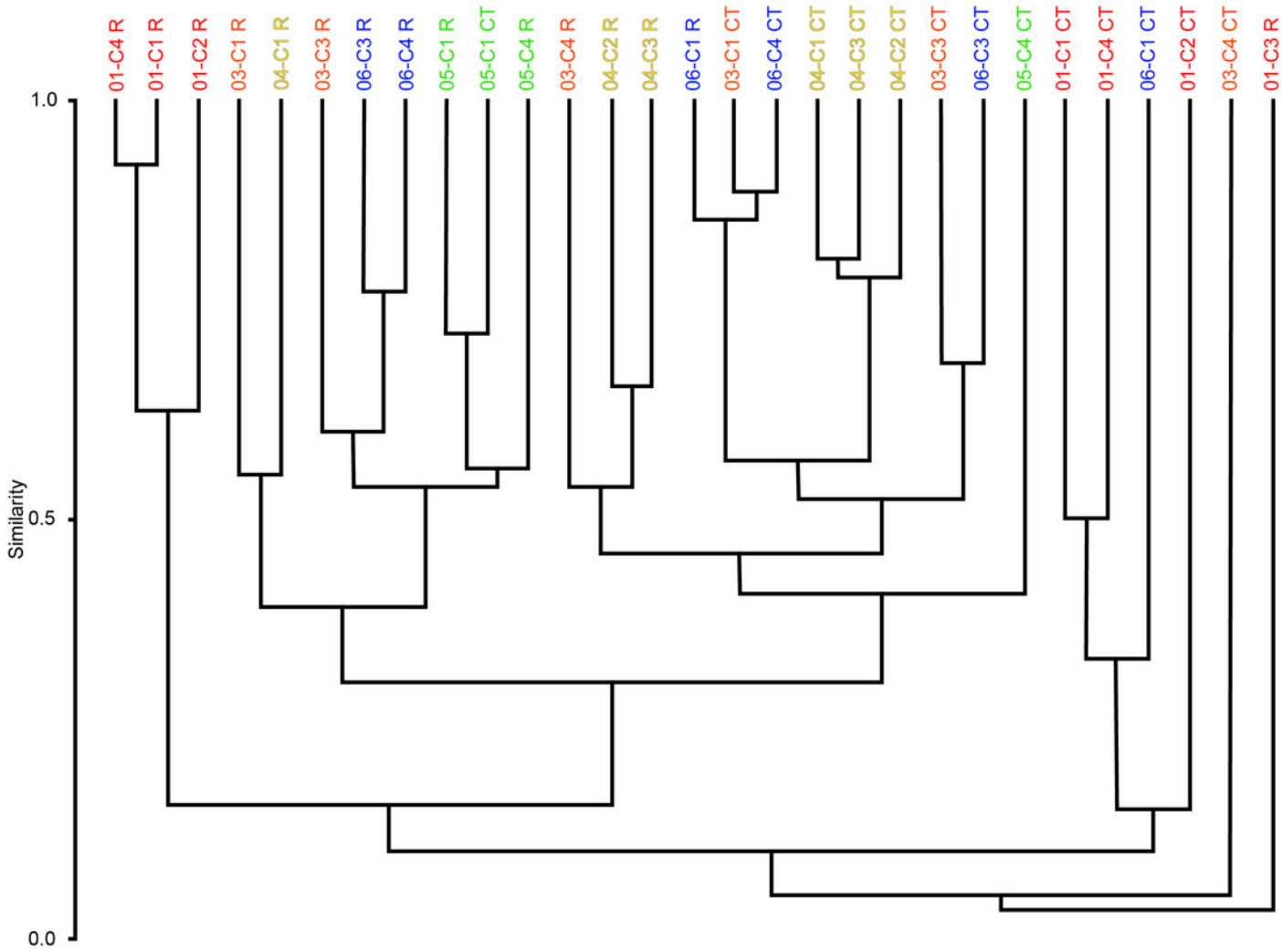

Table 1(on next page)

Jacobs et al Table 1

Table 1. Summary of horizons and samples used in this study.

Horizon	Latitude	Longitude	Core Samples from Horizon	Notes
EB18-01	38.9969°N	78.3748°W	C1, C2, C3, C4	~0.5 m above contact between Lincolnshire LS and Edinburg Fm
EB18-03	38.9968°N	78.3744°W	C1, C3, C4	~20-30 m up section from EB18-01
EB18-04	—	—	C1, C2, C3	0.5 m up section from EB18-03
EB18-05	—	—	C1, C4	1.0 m up section from EB18-04
EB18-06	—	—	C2, C3, C4	~5 m up section from EB18-05

1

Table 2(on next page)

Jacobs et al Table 2

Table 2. Anatomical measurements and classifications by taxon and sclerite. Measurements taken from CT and residue imagery for each of several common taxa. The main sclerites of trilobites (excluding hypostomes and librigenae) were assigned different sets of measurements due to fundamental differences in structure. Lengths, widths, and heights are measured in mm; angles are measured in degrees; other category variables were recorded as Booleans. * Raphiophorids have an effaced prosopon with indistinct furrows, making identification of the occipital lobe difficult in CT especially. For this family of trilobites, occipital width was instead measured as the full width (tr.) of the sclerite from gena to gena at the occiput. ** For eyeless trilobites of the families Metagnostidae and Raphiophoridae, interocular distance was excluded. *** This is the angle formed at the apex between the axis of coiling and a line tangent to the outer walls of the body whorls.

Taxon		Measurements and Classifications
Trilobita	Cranidium	Maximum width (tr.) of occipital lobe*, maximum width (tr.) between eyes**, total length (sag.)
	Thoracic segment	Maximum width (tr.) of axial ring, width (tr.) between fulcra of left and right pleurae, length (sag.) of axial ring
	Pygidium	Maximum width (tr.) of first axial ring, total length (sag.)
Bryozoa		Growth form: dendroid or fenestrate
Gastropoda		Presence/absence of outer walls of whorls, total height of shell, height of last complete whorl, width of last complete whorl, half-angle of teleoconch***
Ostracoda		Body length (a.-p.), body height (d.-v.), articulation/disarticulation, presence/absence of lateral spine

1

Table 3(on next page)

Jacobs et al Table 3

Table 3. Fossils Recovered by Preparation Method and Taxon. Total counts of all objects identified in CT and residue imagery, grouped by taxon. Trilobites are further broken down to the family level. Trilobite material lacking sufficient anatomical features to be confidently assigned to a family was given its own category.

Taxon		µCT	Residues
Total Trilobita		225	594
Trilobita	Asaphidae	6	20
	Cheiruridae	2	3
	Metagnostidae	6	14
	Odontopleuridae	0	18
	Pterygometopidae	6	41
	Raphiophoridae	57	149
	Remopleurididae	22	59
	Unknown Trilobita	126	290
Bivalvia		2	1
Brachiopoda		0	5
Bryozoa	Thin branching	9	304
	Thick branching	0	49
	Fenestrate	7	22
Gastropoda		10	11
Ostracoda		1	232
Unknown		327	161
Total		**581**	**1379**

1

Table 4(on next page)

Jacobs et al Table 4

Table 4. Taxonomic Effects on Recovery. Contingency table containing counts of fossils with distinctive geometry identified in CT imagery and either recovered or not recovered in residue. Residuals of recovered counts are standardized to the expected number of recovered specimens for a taxon; positive residuals indicate disproportionately high likelihood of recovery in residues, while negative values indicate lower-than-average likelihood of recovery. Statistically significant results ($p < 0.05$) are shaded.

Taxon	Not Recovered	Recovered	Recovered residual	p-value
Asaphidae	3	2	0.213	0.84
Cheiruridae	1	1	0.285	0.67
Metagnostidae	2	4	1.855	0.11
Pterygometopidae	4	1	-0.787	0.46
Raphiophoridae	37	20	-0.376	0.90
Remopleurididae	13	8	0.493	0.81
Unknown Trilobita	71	28	-7.389	0.04
Bivalvia	1	1	0.285	0.67
Bryozoa (thin)	4	4	1.140	0.39
Bryozoa (fenestrate)	2	4	1.855	0.11
Gastropoda	4	6	2.425	0.10

1

Table 5(on next page)

Jacobs et al Table 5

Table 5. Comparison of Taxonomic Abundances. Contingency table containing total counts of taxa identified in CT and in residue imagery. Residuals of recovered counts are standardized to the expected number of recovered specimens for the combination of taxon and preparation; positive CT residuals indicate overrepresentation in CT for that taxon, while positive residue residuals indicate overrepresentation in residues (relative to average proportional abundance for all fossils). Statistically significant results ($p < 0.05$) are shaded.

Taxon	CT	Residue	CT residual	Residue residual	p-value
Asaphidae	6	20	0.715	-0.326	0.43
Cheiruridae	2	3	1.224	-0.559	0.18
Metagnostidae	6	14	1.372	-0.627	0.13
Odontopleuridae	0	18	-1.762	0.805	0.05
Pterygometopidae	6	41	-0.741	0.338	0.41
Raphiophoridae	57	149	3.598	-1.643	2.0 E-05
Remopleurididae	22	59	2.146	-0.980	0.02
Unknown Trilobita	126	290	6.399	-2.922	9.9 E-17
Bivalvia	2	1	2.060	-0.941	0.02
Brachiopoda	0	5	-0.929	0.424	0.31
Bryozoa (thin)	9	304	-6.125	2.797	3.3 E-14
Bryozoa (thick)	0	49	-2.908	1.328	1.2 E-3
Bryozoa (fenestrate)	7	22	0.892	-0.407	0.32
Gastropoda	10	11	3.350	-1.530	2.1 E-4
Ostracoda	1	232	-6.183	2.824	1.3 E-13

1

Table 6(on next page)

Jacobs et al Table 6

Table 6. Abundance of taxonomic groups identified in CT data used in NMDS.

	01-C1	01-C2	01-C4	03-C1	03-C3	03-C4	04-C1	04-C2	04-C3	05-C1	05-C4	06-C1	06-C3	06-C4	**Sum**
Agnostida	0	0	0	1	0	0	1	2	0	1	0	0	0	1	**6**
Asaphidae	0	0	0	0	0	1	2	0	1	1	1	0	0	0	**6**
Cheiruridae	0	0	0	0	0	0	0	0	0	1	1	0	0	0	**2**
Odontopleuridae	0	0	0	0	0	0	0	0	0	0	0	0	0	0	**0**
Pterygometopidae	0	0	0	0	0	0	1	1	0	3	0	0	0	1	**6**
Raphiophoridae	0	0	0	3	1	0	5	4	5	23	14	0	0	2	**57**
Remopleuridae	0	0	1	0	5	1	2	1	5	4	1	0	2	0	**22**
Trilo indet	2	0	1	8	12	0	19	15	16	31	5	2	6	9	**126**
Bivalvia	0	0	0	0	1	0	0	0	0	0	0	0	1	0	**2**
Brachiopoda	0	0	0	0	0	0	0	0	0	0	0	0	0	0	**0**
Bryo thin	3	1	2	1	0	0	0	0	0	0	1	0	0	1	**9**
Bryo thick	0	0	0	0	0	0	0	0	0	0	0	0	0	0	**0**
Bryo fenestrate	1	0	6	0	0	0	0	0	0	0	0	0	0	0	**7**
Gastropoda	0	0	0	0	3	0	2	1	0	0	0	0	4	0	**10**
Ostracoda	0	0	0	0	0	0	0	1	0	0	0	0	0	0	**1**
SUM	**6**	**1**	**10**	**13**	**22**	**2**	**32**	**25**	**27**	**64**	**23**	**2**	**13**	**14**	

1

Table 7 (on next page)

Jacobs et al Table 7

Table 7. Abundance of taxonomic groups recovered in acid maceration residues used in NMDS.

	01-C1	01-C2	01-C3	01-C4	03-C1	03-C3	03-C4	04-C1	04-C2	04-C3	05-C1	05-C4	06-C1	06-C3	06-C4	**Sum**
Agnostida	0	0	0	0	6	2	0	2	1	0	0	0	0	2	1	**14**
Asaphidae	0	0	0	0	0	2	1	4	1	2	0	0	0	4	6	**20**
Cheiruridae	0	0	0	0	1	0	0	0	0	1	0	1	0	0	0	**3**
Odontopleuridae	0	0	0	0	9	0	0	4	1	0	3	0	0	0	1	**18**
Pterygometopidae	0	0	0	0	12	4	0	5	2	0	1	5	1	4	7	**41**
Raphiophoridae	0	0	0	0	59	8	1	21	7	2	19	12	2	10	8	**149**
Remopleuridae	0	1	0	0	8	30	0	6	2	2	2	0	0	4	4	**59**
Trilo indet	2	8	0	2	72	51	6	22	17	8	37	12	8	29	16	**290**
Bivalvia	0	0	0	0	0	1	0	0	0	0	0	0	0	0	0	**1**
Brachiopoda	0	0	0	1	2	0	0	0	1	0	1	0	0	0	0	**5**
Bryo thin	42	81	0	43	17	24	0	0	6	3	11	13	0	36	28	**304**
Bryo thick	8	8	4	15	4	0	1	0	0	0	0	0	0	7	2	**49**
Bryo fenestrate	10	0	0	9	2	0	0	0	0	0	0	0	0	0	1	**22**
Gastropoda	0	0	0	0	0	6	0	0	0	0	0	0	0	5	0	**11**
Ostracoda	0	3	1	0	57	15	6	110	13	10	9	4	0	2	2	**232**
SUM	**62**	**101**	**5**	**70**	**249**	**143**	**15**	**174**	**51**	**28**	**83**	**47**	**11**	**103**	**76**	

1